Band structure and quantum Poincaré sections
of a classically chaotic quantum rippled channel

G. A. Luna-Acosta,* Kyungsun Na, and L. E. Reichl

Center for Studies in Statistical Mechanics and Complex Systems, The University of Texas at Austin, Austin, Texas 78712

A. Krokhin

Instituto de Fisica, Universidad Autonoma de Puebla, Puebla, Mexico 72570

(Received 24 July 1995)

We obtain the energy band spectra, eigenfunctions, and quantum Poincaré sections of a free particle moving in a two-dimensional channel bounded by a periodically varying (ripple) wall and a flat wall. Classical Poincaré sections show a generic transition from regular to chaotic motion as the size of the ripple is increased. The energy band structure is obtained for two representative geometries corresponding to a wide and a narrow channel. The comparison of numerical results with the level-splitting predictions of low-order quantum degenerate perturbation theory elucidate some aspects of the classical-quantum correspondence. For larger ripple amplitudes the conduction bands for narrow channels become flat and nearly equidistant at low energies. Quantum-classical correspondence is discussed with the aid of quantum Poincaré (Husimi) plots.

PACS number(s): 05.45.+b, 73.20.Dx, 03.65.−w

I. INTRODUCTION

Investigations on the classical and quantum mechanics of particles in billiards have been very fruitful from the academic as well as from the technological standpoint. On one hand, billiards such as the Buminovich and Sinai billiards have served as paradigms for studying general dynamical features of deterministic chaotic systems [1–3]. The quantum and semiclassical treatments of these and other billiards have also contributed greatly to the understanding of the quantum manifestations of classical chaos [4,5] and quantum transport [6]. On the other hand, billiards, open and closed, can also be realized experimentally in mesoscopic ballistic systems [7–9], in magnetic billiards [10], and in microwave cavities [11].

Two-dimensional electron waveguides or channels also form billiards in the ballistic regime. Kouwenhoven et al. fabricated such a system with a sequence of 15 quantum dots [12], yielding a rectangular sawtooth wall that varies periodically between two values. Quantum mechanical ballistic calculations have explained some transport and magnetotransport properties of this system [13]. Profiles of this and other shapes may be fabricated in mesoscopic systems using submicrometer lithography or by the appropriate application of gate voltages [14]. They may also be realized as films whose thickness is a periodic function of the coordinates or as an inversion layer with a periodically modulated surface [15].

Classical ballistic transport quantities have been calculated recently for a finite rippled sinusoidal channel [16]. The contribution of chaotic and regular motion to transport was identified explaining the dynamical origin of certain transport properties. Quantum mechanical calculations for the infinitely long rippled channel have been carried out numerically [13] and analytically in the weak binding approximation [17]. However, these investigations did not make any connection or identification with the underlying regular and chaotic dynamics of the classical model.

The energy spectrum for the quantum ripple channel has band structure. The band structure is dependent on the parameters of the channel; consequently, one may study the correlation between level repulsion and the dynamical features of the classical system. Moreover, using the Bloch momentum as a tunable parameter, the level statistics can be calculated to further characterize the system and to check the universal predictions of quantum chaos based on level spacing properties [18,19]. Such an analysis was carried out recently [20] for a simple real Si crystal, where the electron can be viewed as a particle in a periodic billiard structure with soft walls (muffin-tin approximation).

In this paper we attempt to relate features in the band structure and energy eigenstates for the quantum ripple channel to the underlying resonance structure and chaos in the classical ripple channel. In Sec. II we present Poincaré plots of the classical channel for two distinct geometries: a narrow and a wide channel. We shall see the various types of dynamics resulting from the variation of the ripple amplitude. In Sec. III we solve the stationary Schrödinger equation to obtain the energy-band structure of the infinitely long rippled channel. This is accomplished by solving the energy eigenvalue problem in curvilinear coordinates where the boundaries of the channel are flat and the Hamiltonian acquires coordinate and

---
*On leave from Instituto de Fisica, Universidad Autonoma de Puebla, Puebla, Mexico, 72570.

momentum dependent terms. In Sec. IV we compare the numerical results with the predictions of degenerate perturbation theory in the appropriate energy range. We find excellent agreement in some cases and drastically different results for other cases. In Sec. V we consider the case of large ripples and high energies. Quantum Poincaré plots are presented in Secs. IV and V to discuss the classical-quantum correspondence of the rippled channel. Finally, in Sec. VI we make some concluding remarks.

II. THE CLASSICAL RIPPLED CHANNEL

The geometry of the classical rippled channel is shown in Fig. 1. the particle bounces back and forth between the flat wall located at $y = 0$ and the periodically rippled wall centered at $y = d$. The profile of the rippled wall is given by

$$y = d + a\cos(x), \tag{1}$$

where d is the average width of the channel and a is the amplitude of the rippled profile. Collisions by the particle with these boundaries are assumed to be specular. A Poincaré map of the trajectory (x_n, α_n) of the particle is straightforward to compute and is given by (ignoring multiple collisions with the ripple)

$$\alpha_{n+1} = \alpha_n + 2\psi_n, \tag{2}$$

$$x_{n+1} = x_n + [d + a\cos(x_n^*)][\tan(\alpha_n) + \tan(\alpha_{n+1})], \tag{3}$$

with

$$\psi_n = \tan^{-1}\left(\frac{\partial}{\partial x}[d + a\cos(x)]\right)\Bigg|_{x=x_n^*}, \tag{4}$$

where x_n is the position on the flat wall at $y = 0$, where the particle hits on the nth bounce, α_n is the angle the particle trajectory makes with the vertical at $x = x_n$, and $\tan(\psi_n)$ is the slope of the tangent to the ripple wall at the point of contact $x = x_n^*$ after the nth bounce (cf. Fig. 1). The discrete time evolution of the Poincaré-Birkhoff variables (x_n, α_n) yields a Poincaré map of the dynamics

of the particle in the ripple channel. An alternative set of variables is the conjugate pair (x_n, p_{xn}), where $p_{xn} = p\sin(\alpha_n)$ is the x component of the momentum right after the nth collision. The magnitude of the total momentum is $p = \sqrt{2E}$, where E is the (conserved) total kinetic energy of the particle. In this paper, we choose mass $m = 1$. Thus, if the particle in the ripple channel is an electron, then all quantities are measured in atomic units.

It is useful to note that different mappings (surfaces of section) for this system have been used. Tennyson [21] introduced this model and chose x_n and α_n to describe the position and the direction of the particle as it bounces off the ripple surface instead of the flat surface and in [16] the complement of this angle was used. Here our surface of section is the flat wall $y = 0$ as this will prove convenient when we connect with the quantum Poincaré plots (described in a later section), which also measure the coordinates relative to the flat surface.

In this paper we shall consider two distinct, representative, geometries: a narrow channel and a wide channel, both of periodicity $L = 2\pi$. For the narrow channel we will choose a width $d = 2\pi/10$. For the wide channel we will choose a width $d = 3\pi$. The various dynamical features of these two representative cases have been studied previously in detail [16] in connection with classical ballistic transmission. In Figs. 2(a)–2(d) we show the Poincaré surfaces of section for the narrow channel with ripple sizes $a = 0$, $a = 2\pi/1000$, $a = 2\pi/50$, and $a = 2\pi/25$, respectively. Note that in these plots we have rescaled the x component of the momentum to $p_{xn}/p = \sin(\alpha_n)$. At $a = 0$, the trajectories are straight lines, indicating the conservation of the x component of momentum in addition to the energy. The situation changes drastically when we begin to turn on the ripple. A large primary resonance zone forms as soon as a becomes different from zero. The large primary resonance at the center is due to the librational motion about $x = 0$, the maximum width of the channel. As the ripple amplitude increases, many of the horizontal Kolmogorov-Arnol'd-Moser (KAM) curves disappear and the separatrix becomes chaotic. For $a = \frac{2\pi}{50}$, there are still some KAM curves prohibiting the connection between the three chaotic regions observed in Fig. 2(c).
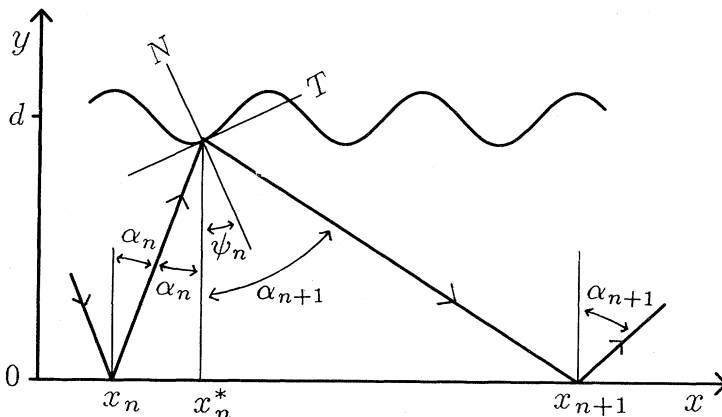

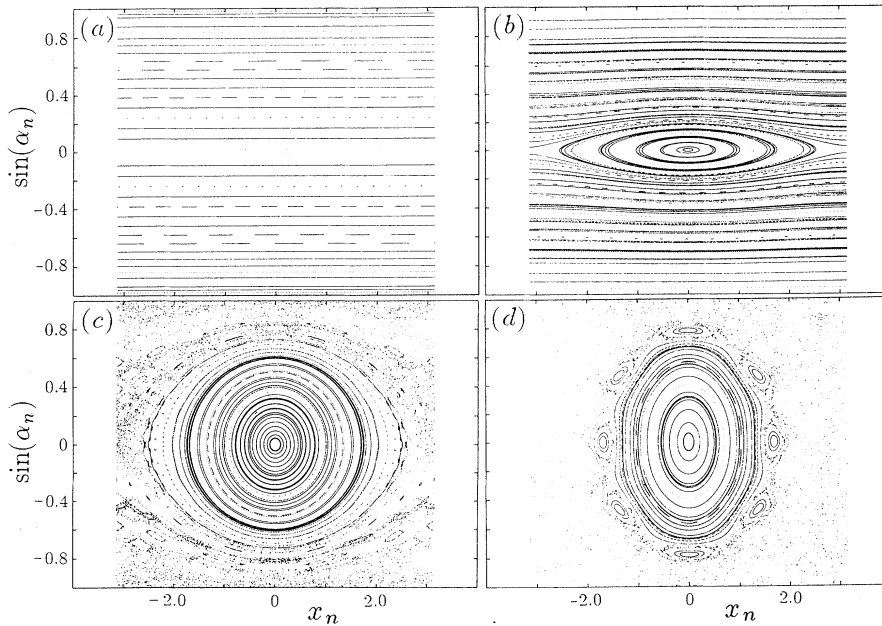FIG. 1. Geometry of the ripple channel (in a.u. for electrons).

FIG. 2. Poincaré surfaces of section for the narrow channel with $d = \frac{2\pi}{10}$ and (a) $a = 0$, (b) $a = \frac{2\pi}{1000}$, (c) $a = \frac{2\pi}{50}$, and (d) $a = \frac{2\pi}{25}$ (in a.u.).

The last KAM curve breaks at around $a = 2\pi/42$ and for larger amplitudes of ripple, e.g., $a = 2\pi/25$, the principal first-order resonance island is surrounded by a chaotic sea. Clearly, all orbits lying inside the central resonance island in Figs. 2(a)–2(d) classically do not contribute to transmission; they are localized within a unit cell in the infinite rippled channel.

In Figs. 3(a)–3(d) we show the Poincaré surfaces of section for the wide channel for ripple sizes $a = 2\pi/1000$, $a = 2\pi/300$, $a = 2\pi/100$, and $a = 2\pi/25$. Notice that in contrast with the narrow channel, several first-order resonance islands, in addition to the central one, are clearly

discernible. Notice that already for small values of the ripple amplitude the overlap of resonances occurs, giving rise to the chaotic zones observed in Fig. 3(b). In Figs. 3(a) and 3(b), the chaotic orbits with positive momentum do not mix with the chaotic orbits with negative momentum, except for those falling on the central chaotic separatrix, which is very thin. This means that most particles moving forward, chaotically or regularly, will not change direction. Increasing the ripple amplitude further causes more and more KAM curves to break and finally produces global chaos, even for fairly small values of the ripple amplitude [see Fig. 3(c)].
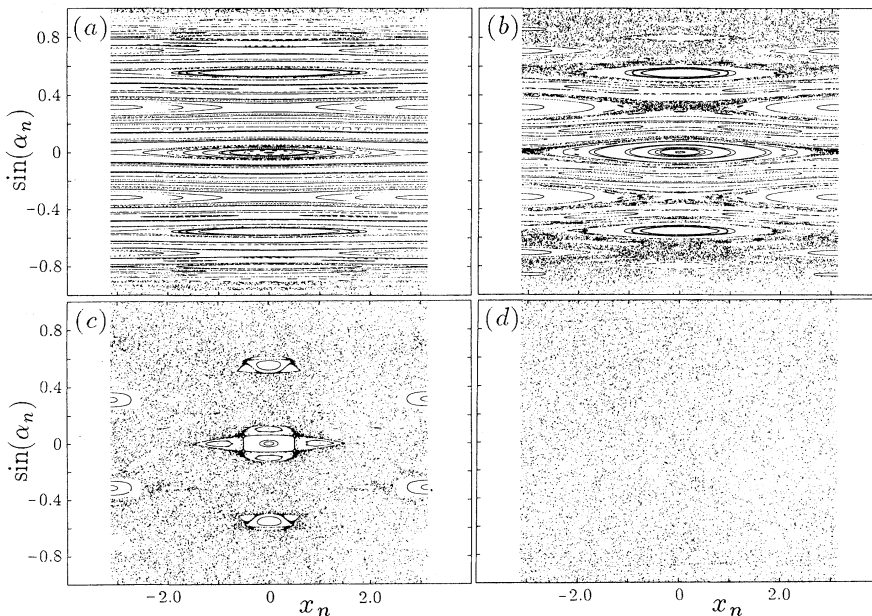

FIG. 3. Poincaré surfaces of section for the wide channel with $d = 3\pi$ and (a) $a = \frac{2\pi}{1000}$, (b) $a = \frac{2\pi}{300}$, (c) $a = \frac{2\pi}{100}$, and (d) $a = \frac{2\pi}{25}$ (in a.u.).

III. THE QUANTUM RIPPLED CHANNEL

Let us now consider the quantum version of this system. We wish to see how the energy eigenvalues and eigenstates are affected by the resonances and chaos. We will transform to a set of curvilinear coordinates and then compute the Hamiltonian matrix for the quantum system and obtain from it the energy spectrum and eigenstates.

A. Coordinate frames

The top and bottom profiles of the channel are given, respectively, by

$$y = d + a\xi(x), \quad y = 0, \tag{5}$$

where $\xi(x) = \xi(x + 2\pi)$ is any periodic function of period 2π. Later we shall specialize to $\xi(x) = \cos(x)$. Although the Hamiltonian $\hat{H}$ is simply the kinetic energy, the quantum particle experiences an effective nonuniform potential due to the confining walls. The energy eigenvalue problem is to be solved subject to Dirichlet boundary conditions (hard walls). Since the walls are not both planar it is convenient to consider two different sets of coordinates: Cartesian coordinates (x, y) and curvilinear coordinates $\mathbf{q} \equiv (q^1, q^2)$.

The covariant coordinate representation of the kinetic energy is given by [22]

$$\langle \mathbf{q} | \hat{H} | \mathbf{q} \rangle = \frac{1}{2} g^{-1/4} P_\alpha g^{1/2} g^{\alpha\beta} P_\beta g^{-1/4}, \tag{6}$$

where the covariant momenta are

$$P_\alpha = -i\hbar \left[\partial_\alpha + \frac{1}{4} \partial_\alpha \ln(g) \right] = -i\hbar g^{-1/4} \partial_\alpha g^{1/4}. \tag{7}$$

Here $\partial_\alpha \equiv \frac{\partial}{\partial q^\alpha}$ $(\alpha, \beta = 1, 2)$. $g_{\alpha\beta}$ is the metric tensor and $g = \text{Det}(g_{\alpha\beta})$ is the metric of the coordinate system (q^1, q^2) (they will be specified below). The Einstein summation convention of repeated indices will be assumed throughout. Substitution of Eq. (7) into Eq. (6) gives the kinetic energy in terms of the covariant Laplacian Δ_{cov} [23]

$$\langle \mathbf{q} | \hat{H} | \Psi_E \rangle = -\frac{\hbar^2}{2} \Delta_{\text{cov}} \Psi_E(\mathbf{q})$$
$$\equiv -\frac{\hbar^2}{2} g^{-1/2} \partial_\alpha g^{\alpha\beta} g^{1/2} \partial_\beta \Psi_E(\mathbf{q}), \tag{8}$$

Note that the wave functions $\Psi_E(\mathbf{q})$ are normalized as

$$\int\int \sqrt{g} \, dq^1 dq^2 \Psi_E^*(\mathbf{q}) \Psi_E(\mathbf{q}) = 1, \tag{9}$$

with the completeness relation

$$\hat{1} = \int\int \sqrt{g} dq^1 dq^2 |\mathbf{q}\rangle\langle\mathbf{q}|, \tag{10}$$

and the integrals are taken over the entire range of coor-

dinate values.

In Cartesian coordinates the familiar forms are obtained

$$\langle x, y | \hat{H} | \Psi_E \rangle = \langle x, y | \frac{1}{2}(p_x^2 + p_y^2) | \Psi_E \rangle$$
$$= E\Psi_E(x, y) = -\frac{\hbar^2}{2}(\partial_x^2 + \partial_y^2)\Psi_E(x, y), \tag{11}$$

where the solution $\Psi_E(x, y)$ must satisfy the boundary conditions

$$\Psi_E(x, y = 0) = 0, \quad \Psi_E[x, y = d + a\xi(x)] = 0. \tag{12}$$

If we transform to curvilinear coordinates $(q^1 = u, q^2 = v)$ such that (see also [15,17, [24]])

$$u = x, \quad v = \frac{y}{d + a\xi(x)}, \tag{13}$$

then the boundaries appear flat,

$$\Psi_E(u, v) = 0 \quad \text{at} \quad v = 0, 1 \tag{14}$$

but the Schrödinger equation acquires coordinate and momentum dependent terms

$$-\frac{\hbar^2}{2}\left(\frac{\partial^2}{\partial u^2} + h_1 \frac{\partial^2}{\partial v^2} + h_2 \frac{\partial^2}{\partial u \partial v} + h_3 \frac{\partial}{\partial v}\right)\Psi_E(u, v)$$

$$= E_\alpha \Psi_E(u, v), \tag{15}$$

where

$$h_1 = \frac{1 + a^2 v^2 \xi_u^2}{(d + a\xi)^2},$$
$$h_2 = \frac{-2av\xi_u}{(d + a\xi)}, \tag{16}$$
$$h_3 = \frac{-av\xi_{uu}}{(d + a\xi)} + \frac{2a^2 v \xi_u^2}{(d + a\xi)^2}.$$

Here $\xi_u \equiv \frac{\partial\xi}{\partial u}$ and the metric tensor and metric are, respectively,

$$g^{\alpha\beta} = \begin{pmatrix} 1 & \frac{-av\xi_u}{(d+a\xi)} \\ \frac{-av\xi_u}{(d+a\xi)} & \frac{1+a^2 v^2 \xi_u^2}{(d+a\xi)^2} \end{pmatrix}, \tag{17}$$

$$g \equiv \text{Det}[g_{\alpha\beta}] = [d + a\xi(u)]^2 = J^2. \tag{18}$$

J is the Jacobian of the transformation in Eq. (13).

B. Bloch states

Because the Hamiltonian is a periodic function of coordinate u, the energy eigenstates will satisfy Bloch's theorem and have the form

$$\Psi_E(u, v) = e^{iku}\varphi_k(u, v), \tag{19}$$

where k is the Bloch wave vector $k = k(E)$ and the state $\varphi_k(u, v)$ is the Bloch function with the periodicity of the

wall $\varphi_k(u + 2\pi, v) = \varphi_k(u, v)$. The solution must satisfy the boundary conditions $\varphi_k(u, 0) = \varphi_k(u, 1) = 0$. If we are describing a periodic flat channel of length $L = 2\pi N$, then the allowed values of the Bloch wave vector are $k = 0, \pm\frac{1}{N}, ..., \pm\frac{(N-1)}{N}$. For an infinite channel, the Bloch wave vector takes a continuous range of values. We choose the first Brillouin zone to lie in the interval $-\frac{1}{2} \le k \le \frac{1}{2}$.

We can expand the Bloch function $\varphi_k(u, v)$ in a Fourier series and write the energy eigenstate as

$$\Psi_E(u, v) = \pi^{-1/2} g^{-1/4} e^{iku}$$
$$\times \sum_{m=1}^{\infty} \sum_{n=-\infty}^{\infty} B_{m,n}^k \sin(m\pi v) e^{inu}, \qquad (20)$$

where the factor $\pi^{-1/2} g^{-1/4}$ arises from the orthonormality condition in curvilinear coordinates, Eq. (9). Thus the energy wave function is expanded in a complete orthonormal basis set, satisfying the boundary conditions of the problem (i.e., a Galerkin series expansion [25]),

$$\Psi_E(u, v) = \sum_{m=1}^{\infty} \sum_{n=-\infty}^{\infty} B_{mn}^k \beta_{mn}^k(u, v), \qquad (21)$$

with

$$\beta_{mn}^k(u, v) \equiv \pi^{-1/2} g^{-1/4} \sin(m\pi v) e^{i(k+n)u}, \qquad (22)$$

where $g^{-1/4} = [d + a\xi(u)]^{-1/2}$.

C. Matrix representation and energy band structure

We now proceed to solve the energy eigenvalue problem by diagonalizing the Hamiltonian Eq. (15) in the Galerkin basis β_{mn}^k,

$$\sum_{m'=1}^{\infty} \sum_{n'=-\infty}^{\infty} H_{mnm'n'} B_{m',n'}^k = E(k) B_{m,n}^k, \qquad (23)$$

where the matrix elements are

$$H_{mnm'n'}^k \equiv \langle mn|\hat{H}|m'n'\rangle_k = -\frac{\hbar^2}{2} \int_0^{2\pi} du \int_0^1 dv\, g^{1/2} (\beta_{mn}^k)^* \Delta_{\text{cov}} \beta_{m'n'}^k$$

$$= -\frac{\hbar^2}{2\pi} \int_0^{2\pi} du \int_0^1 dv \sin(m\pi v) e^{-i(k+n)u} g^{-1/4} \partial_\alpha g^{1/2} g^{\alpha\beta} \partial_\beta \sin(m'\pi v) e^{i(k+n')u} g^{-1/4}. \qquad (24)$$

Integration by parts yields

$$H_{mnm'n'}^k = \frac{\hbar^2}{2\pi} \int_0^{2\pi} du \int_0^1 dv \partial_\alpha [\sin(m\pi v) e^{-i(n+k)u} g^{-1/4}] g^{1/2} g^{\alpha\beta} \partial_\beta [\sin(m'\pi v) e^{i(n'+k)u} g^{-1/4}], \qquad (25)$$

which can readily be checked to be Hermitian since $g^{\alpha\beta} = g^{\beta\alpha}$. Let us now specify $\xi(u) = \cos(u)$. Then, after some algebra and calculus, we find

$$H_{mnm'n'}^k = \frac{\hbar^2}{2} (n + k)^2 \delta_{mm'} \delta_{nn'} + \frac{\hbar^2}{2\pi} \left(\frac{1}{2} (m^2 \pi^2) J_{nn'}^3 + \frac{a^2}{6} (m^2 \pi^2) J_{nn'}^4 + \frac{a^2}{8} J_{nn'}^4 \right) \delta_{mm'}$$

$$+ \frac{\hbar^2}{2\pi} \left[(-ai)(-1)^{m+m'} \frac{mm'}{m^2 - m'^2} (n + n' + 2k) J_{nn'}^5 + a^2 (-1)^{m+m'} \left(\frac{2(m^2 + m'^2)}{(m'^2 - m^2)^2} \right) J_{nn'}^4 \right], \qquad (26)$$

where $J_{nn'}^3$, $J_{nn'}^4$, $J_{nn'}^5$ are given by the integrals

$$J_{nn'}^3 = \int_0^{2\pi} du \frac{e^{i(n-n')u}}{[d + a\cos(u)]^2} = \frac{2\pi}{(d^2 - a^2)} \left(\frac{\sqrt{d^2 - a^2} - d}{a} \right)^{|n-n'|} \left(\frac{d}{\sqrt{d^2 - a^2}} + |n - n'| \right), \qquad (27)$$

$$J_{nn'}^4 = \int_0^{2\pi} du \frac{e^{i(n-n')u} \sin^2(u)}{(d + a\cos u)^2} = \frac{\pi}{(d^2 - a^2)} \left[\left(\frac{\sqrt{d^2 - a^2} - d}{a} \right)^{|n-n'|} \left(\frac{d}{\sqrt{d^2 - a^2}} + |n - n'| \right) \right.$$

$$\left. - \frac{1}{2} \sum_{l=2,-2} \left(\frac{\sqrt{d^2 - a^2} - d}{a} \right)^{|n-n'+l|} \left(\frac{d}{\sqrt{d^2 - a^2}} + |n - n' + l| \right) \right], \qquad (28)$$

and

$$J_{nn'}^5 = \int_0^{2\pi} du \frac{e^{i(n-n')u} \sin(u)}{(d + a\cos u)} = \frac{i\pi}{\sqrt{d^2 - a^2}} \left[\left(\frac{\sqrt{d^2 - a^2} - d}{a} \right)^{|n-n'-1|} - \left(\frac{\sqrt{d^2 - a^2} - d}{a} \right)^{|n-n'+1|} \right]. \qquad (29)$$

For the flat channel ($a = 0$), Eq. (26) reduces to

$$H^k_{mm'nn'} = \frac{\hbar^2}{2}\left((n+k)^2 + \frac{m^2\pi^2}{d^2}\right)\delta_{mm'}\delta_{nn'}. \quad (30)$$

Diagonalization is carried out using a matrix with columns and rows labeled by the pairs $l = (m, n)$ and $l' = (m'n')$. Convergence is checked as usual by increasing the matrix size until no changes in the eigenvalues occur.

Figures 4(a) and 5(a) show the band structures, in the reduced first Brillouin zone (BZ) scheme, for the narrow and wide *flat* channels, respectively. Figure 4(b) shows the effect of a small ripple on the band structure of the narrow channel. Note the large splittings at the center and edges of the BZ. For convenience, the energy E is plotted relative to $E^0_1(0) = \frac{\hbar^2}{2}\left(\frac{\pi}{d}\right)^2$. For the narrow channel, the dispersion curves appear linear. For the flat case and approximately for the small ripple case, the dispersion relation is $E_m(k) \approx \frac{\hbar^2}{2}[(k+n)^2 + (\pi m/d)^2]$. Since $(\pi m/d)^2 = 25m^2$ for the narrow channel ($d = \frac{2\pi}{10}$), this term dominates the dispersion relation and therefore the k dependence looks linear. On the other hand, for the wide channel where $d = 3\pi$, the familiar parabolic dependence is clear in Fig. 5(a). When the ripple size is small enough its effect on the potential may be considered as a perturbation on the flat channel. In Sec. IV we shall compare our numerical results with the predictions of first-order degenerate perturbation theory.

Figures (6) and 5(b) show the band structure as the ripple size increases for the narrow and wide channels, respectively. For the narrow channel and ripple amplitude $a \geq 2\pi/50$, the level repulsion is so strong at low energies that the spectrum in this region is practically discrete (see Fig. 6). That is, only a narrow range of values
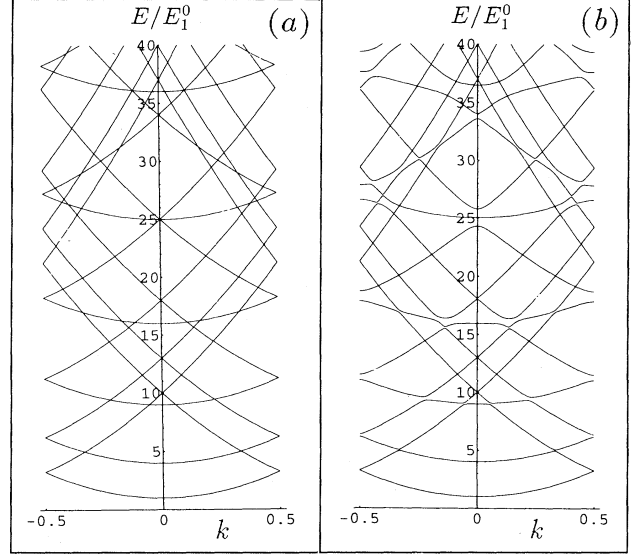

FIG. 5. Energy band structure for the wide channel with $d = 3\pi$ and (a) $a = 0$ and (b) $a = \frac{2\pi}{25}$ (in a.u.).

of the energy are allowed and since the slope of these bands is approximately zero, the group velocity of the particle wave packet is approximately zero. The classical Poincaré map for the narrow channel corresponding to the parameters of Fig. 6(a) is shown in Fig. 2(c) and that corresponding to Fig. 6(b) is shown in Fig. 2(d). For the wide channel [Fig. 5(b)], we see that although avoided crossings occur as the ripple size increases, the band gaps are very few and thin. In Secs. IV and V, we shall discuss features of the spectra in connection with
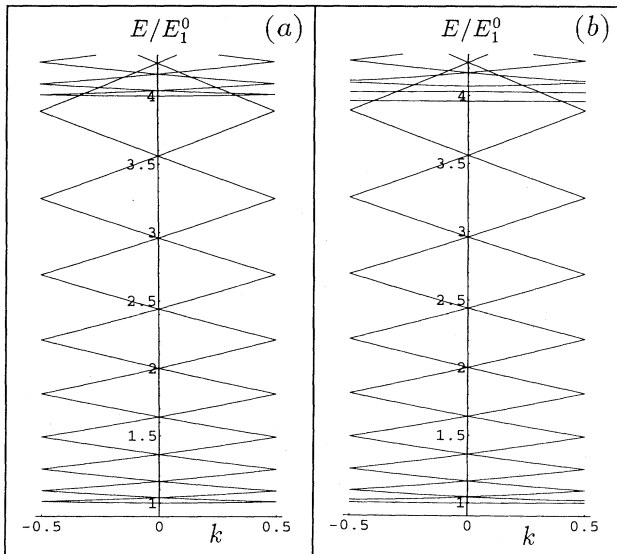

FIG. 4. Energy band structure for the narrow channel with $d = \frac{2\pi}{10}$ and (a) $a = 0$ and (b) $a = \frac{2\pi}{1000}$ (in a.u.).
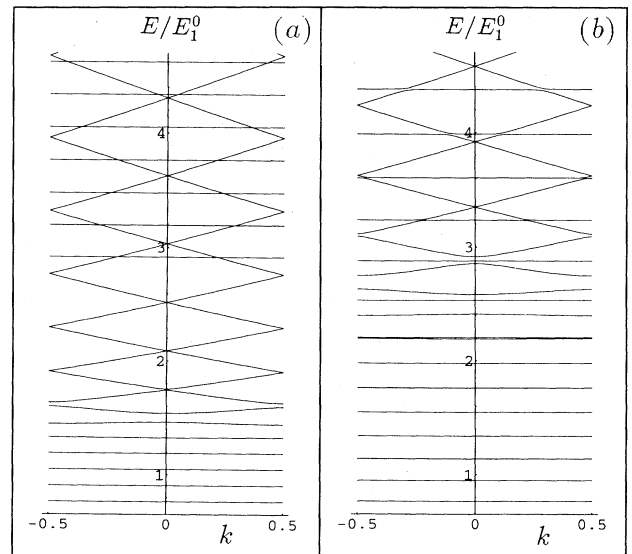

FIG. 6. Energy band structure for the narrow channel with $d = \frac{2\pi}{10}$ and (a) $a = \frac{2\pi}{50}$ and (b) $a = \frac{2\pi}{25}$ (in a.u.).

the classical-quantum correspondence, with the aid of quantum Poincaré maps.

IV. DEGENERATE PERTURBATION THEORY

The Hamiltonian expressed in curvilinear coordinates [cf. Eq. (15)] enables us to use perturbation theory to examine the system for small ripple amplitude. If the ripple amplitude a is small compared to the width d, then $a/d \equiv \epsilon \ll 1$ and the Hamiltonian can be divided into two terms

$$\langle u, v | H | u, v \rangle_{\epsilon \ll 1} \approx [\hat{H}_0(u, v) + V(u, v)], \qquad (31)$$

where

$$\hat{H}_0 = -\frac{\hbar^2}{2}(\partial_u^2 + d^{-2}\partial_v^2) \qquad (32)$$

is the Hamiltonian of a particle moving inside a flat channel and V is the perturbation due to the small ripple. Thus

$$\hat{H}_0 \Psi_m^0(k) = E_m^0(k)\Psi_m^0(k), \qquad (33)$$

with

$$E_m^0(k) = \frac{\hbar^2}{2}\left(k^2 + \frac{m^2\pi^2}{d^2}\right) \qquad (34)$$

and

$$\Psi_m^0(k) = \sqrt{\frac{1}{\pi d}}\, e^{iku} \sin(\pi m v). \qquad (35)$$

Keeping only terms to first-order in ϵ (we can then set $u = x$ and $v = y/d$), we get from Eq. (15)

$$V = \epsilon \frac{\hbar^2}{2}\left(2\xi \frac{\partial^2}{\partial y^2} + 2\xi_x y \frac{\partial^2}{\partial x \partial y} + \xi_{xx} y \frac{\partial}{\partial y}\right), \qquad (36)$$

where now $\xi = \xi(x)$. To zeroth order, electron states are characterized by the continuous x momentum $p_x = \hbar k$ and by the discrete transversal mode m. As soon as the perturbation is turned on, p_x is no longer conserved but, because of the periodicity of V, the continuous Bloch vector k (not equal to $p_x/\hbar$ anymore) is still a constant of the motion. The unperturbed states $\Psi_m^0(k)$ and $\Psi_{m'}^0(k')$ are degenerate if the quantum numbers k, k', m, and m' satisfy the condition

$$k^2 + \frac{m^2\pi^2}{d^2} = k'^2 + \frac{m'^2\pi^2}{d^2}. \qquad (37)$$

In the scheme of the extended Brillouin zones, the dispersion law is periodic in k,

$$E_m^0(k) = E_m^0\left(k + \frac{2\pi s}{L}\right), \qquad s = \pm 1, \pm 2, ..., \qquad (38)$$

where s denotes the sth Brillouin zone and L is the period of $\xi(x)$. Here $L = 2\pi$. Then the Bloch vectors k and k' are related by $k' = k + s$. Substituting this into Eq. (37) gives the following equation for k:

$$2k + s = \left(\frac{\pi}{d}\right)^2 \left(\frac{m^2 - m'^2}{s}\right). \qquad (39)$$

Here the integers m, m', and s are fixed and k lies in the first Brillouin zone $(-\frac{1}{2} \leq k \leq \frac{1}{2})$. It is easy to see from Eq. (39) that if $m = m'$, the center $(k = 0)$ and the edges of the Brillouin zone $(k = \pm\frac{1}{2})$ are degenerate points. Other (accidental) degeneracies, with $m' \neq m$, lie inside the first Brillouin zone. Note that the band spectrum for the narrow flat channel [Fig. 4(a)] does not have accidental degeneracies in the lower part of the spectrum, whereas for the wide flat channel [Fig. 5(a)] it does. Degenerate perturbation theory gives the amount of splitting (level repulsion) that may occur as the boundaries of the channel deviate from being ideally flat. The approximation is expected to be valid when the matrix elements of the perturbation operator V are small compared to the electron energy (see also Ref. [17]).

In our system, degeneracies can occur between two and more levels but by far the most common is a twofold degeneracy as exemplified in Figs. 4(a) and 5(a). For cases of twofold degeneracy, a straightforward calculation using the perturbation potential Eq. (36) yields matrix elements

$$\langle m, k | V | m', k' = k + s \rangle = -2\epsilon E_1^0(0)mm'(-1)^{m+m'}\tilde{\xi}(s)$$

$$\text{for} \quad s = 0, \pm 1, \pm 2, ..., \qquad (40)$$

where

$$\tilde{\xi}(s) \equiv \frac{1}{2\pi}\int_0^{2\pi} dx\, \xi(x) e^{isx} \qquad (41)$$

is the Fourier component for the periodic profile and $E_1^0(0) = \frac{\hbar^2}{2}\left(\frac{\pi}{d}\right)^2$ is the energy of the first transverse mode [cf. Eq. (34)]. Clearly, the diagonal matrix elements $(m = m', s = 0)$ are zero if $\tilde{\xi}(0) = 0$, which is the case, for example, for the trigonometric functions. In this case the perturbed energies to first-order are simply given by

$$E^{\pm} = E_m^0(k) \pm 2\epsilon E_1^1(0)mm'\tilde{\xi}(s) \quad \text{for} \quad s = \pm 1, \pm 2, ... \qquad (42)$$

If we specialize to the cosine profile $\xi(x) = \cos(x)$, then

$$\tilde{\xi}(s) = \frac{1}{2}(\delta_{s,1} + \delta_{s,-1}). \qquad (43)$$

Thus, first-order degenerate perturbation theory predicts, for a cosine profile, a splitting given by

$$\Delta^{(1)} \equiv E^+ - E^- = 2\epsilon E_1^0(0)mm'(\delta_{s,1} + \delta_{s,-1}). \qquad (44)$$

Scaling the energy by $E_1^0(0)$ in accordance with plots of Figs. 4-6 gives the scaled splitting

$$\bar{\Delta}^{(1)} = \frac{\Delta^{(1)}}{E_1^0(0)} = 2\epsilon mm', \quad s = \pm 1. \qquad (45)$$

The corresponding states (to zeroth order) are

$$\Psi^{\pm} = \frac{1}{\sqrt{2\pi d}}[\sin(m\pi y/d) \mp \sin(m'\pi y/d)e^{ix}]e^{ikx}. \quad (46)$$

Equation (43) demonstrates that the harmonic ripple lifts the degeneracy (to first order in ϵ) only when $s = \pm 1$, that is, only for crossings of lines (subbands) from immediately neighboring Brillouin zones ($s = \pm 1$). We see that the splitting of levels depends on the number of Fourier components needed to expand a given ripple profile $\xi(x)$. For example, a rectangular sawtooth profile like the one in the experiments of Kouwenhoven et al. [12] is expected to remove all degeneracies to first order in ϵ. For the common case $m = m'$, the probability density is

$$|\Psi^{\pm}(x,y)|^2 = \frac{1}{\pi d}\sin^2\left(\frac{m\pi y}{d}\right)$$
$$\times \begin{cases} \sin^2(x/2) \\ \cos^2(x/2). \end{cases} \quad (47)$$

Note that the lower energy split state is proportional to $\cos^2(x/2)$. Let us now compare these results with numerical experiments. We shall consider both narrow and wide channels.

A. Wide channel

Let us use the parameters $a = \frac{2\pi}{300}$ and $d = 3\pi$ so that $\epsilon = a/d = 0.0022$. The classical phase space Poincaré map corresponding to these values [cf. Fig. 3(b)] is already a mixed phase space. However, since the matrix elements Eq. (40) are much smaller than the energy in the range considered, quantum degenerate perturbation theory (QDPT) to first order is expected to be valid. Indeed, careful examination of the data, obtained by the numerical calculations of Sec. III C, shows that level repulsion occurs as predicted by Eq. (45). That is, the perturbation potential produces a splitting given by Eq. (45) and only for degenerate states whose k values differ by one. As ϵ increases to $\epsilon = \frac{a}{d} = \frac{2\pi}{25}\frac{1}{3\pi} = 0.0267$, splitting between these neighboring unperturbed states is still given correctly by Eq. (45) for the low lying states ($m, m' < 5$). However, some small repulsion of levels for unperturbed degenerate states whose k values differ by 2 can be observed by close inspection of Fig. 5(b). The classical Poincaré map for these parameters is shown in Fig. 3(d). Thus it appears that first-order QDPT can be used to predict correctly the level repulsion for the lower part of the energy spectrum (low values of m, m').

B. Narrow channel

Let us now consider the narrow channel with parameters $a = \frac{2\pi}{1000} = 0.001$ and $d = 3\pi$ so that $\epsilon = a/d = \frac{2\pi}{1000}\frac{10}{2\pi} = 0.01$. The classical Poincaré map for these values [Fig. 2(b)] is dominated by KAM tori with a pendulum-like structure. The only chaos [not perceptible in Fig. 2(b)] resides on a very narrow layer near

$\sin(\alpha) = 1$ and on the extremely thin chaotic separatrix. Here also QDPT to first-order is expected to apply, but the comparison with the numerical calculations for the band spectrum [Fig. 4(b)] shows very large discrepancies. For example, at $k = 0$, none of the level crossings for the flat channel are supposed to split under first-order QDPT since these belong to degenerate states from Brillouin zones, which are $s=2, 4, 6,...$ zones apart. However, numerical data show that the second and third levels split and as is clearly seen in Fig. 4(b), the 19th and 20th levels also split.

The reason for the discrepancy can be understood by performing second-order QDPT [26]. The calculation now involves the solution of the secular equation $|\tilde{V}_{nn'} - E^{(2)}\delta_{nn'}| = 0$, where $\tilde{V}_{nn'} \equiv \sum_l v_{nl}V_{ln'}/(E_n^0 - E_l^0)$, $|n\rangle \equiv |m, k\rangle$, and $|n'\rangle \equiv |m', k\pm 2\rangle$ are the twofold degenerate states and the summation is over all states not degenerate with $|n\rangle$. Since V_{nl} is zero for $|s| \neq 1$ [cf. Eq. (40)], there are very few terms (one or two) that contribute to the summation over l. We find a splitting of energies given by

$$\Delta^{(2)} \equiv E^+ - E^- = [2\epsilon E_1^0(0)]^2. \quad (48)$$

The scaled splitting is

$$\bar{\Delta}^{(2)} = \frac{\Delta^{(2)}}{E_1^0(0)} = 2\epsilon^2\left(\frac{\pi}{d}\right)^2 \quad \text{for} \quad s = \pm 2. \quad (49)$$

The probability density of the split states is (for $m = m'$)

$$|\Psi^{\pm}(x,y)|^2 = \frac{1}{\pi d}\sin^2\left(\frac{m\pi y}{d}\right)$$
$$\times \begin{cases} \cos^2(x) \\ \sin^2(x). \end{cases} \quad (50)$$

Note that the lower (higher) energy split state has odd (even) parity now, which is opposite the case of splitting between degenerate unperturbed states with $s = \pm 1$.

Equation (49) shows that the validity of QDPT demands not only that the expansion parameter $\epsilon = \frac{a}{d}$ be small, but also that the width of the channel be large enough ($\frac{\pi}{d} < 1$). The comparison of Eq. (49) with numerical data is in excellent agreement only for very small ϵ, e.g., $\epsilon = 0.001$, which is consistent with the requirement that the ratio $\Delta^{(2)}/\Delta^{(1)} = \epsilon(\pi/d)^2$ be much less than one. The value $\epsilon = 0.001$ for the narrow channel meets this requirement and the splitting of levels at $k = 0$ obtained numerically is correctly predicted by Eq. (49). For $\epsilon = 0.01$ [see Fig. 2(b)], where $\Delta^{(2)}/\Delta^{(1)} = 0.25$, the probability density from the numerical experiments (Fig. 7) agrees well with Eq. (50). However, the energy splittings agree only in their order of magnitude and for the low energy spectrum. Moreover, splittings between degenerate states with $s = 4$ are already non-negligible. Thus QDPT, to low orders, does not predict correctly the energy shifts for the case of narrow channels unless the ripple size-to-width ratio $\epsilon = a/d$ is extremely small to ensure convergence.

It is not completely a surprise that first-order QDPT fails for parameter values for the classical Poincaré map
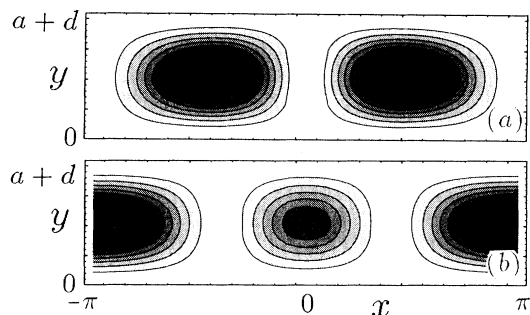
FIG. 7. Energy eigenstates in the x-y plane for the narrow channel with $d = \frac{2\pi}{10}$, $a = \frac{2\pi}{1000}$, $\epsilon = 0.01$, and $k = 0$. These correspond to energy levels (a) 2 and (b) 3 (in a.u.).

FIG. 9. Husimi plots for the narrow channel with $d = \frac{2\pi}{10}$, $a = \frac{2\pi}{1000}$, and $k = 0$. These correspond to energy levels (a) 19 and (b) 20 (in a.u.).

of Fig. 2(b) with a pendulumlike large resonance. The dynamics of a classical particle in this narrow channel is very nearly integrable and pendulumlike. Therefore the preferred basis is the Mathieu functions, whereas QDPT uses a plane wave basis. In fact, if we consider the perturbed one-dimensional Hamiltonian $H = H_0 + \epsilon \cos(x)$, the standard Rayleigh-Schrödinger perturbation is very slowly convergent in terms of the plane wave basis [27]. Moreover, there is no energy shift to first order in ϵ, just as we found for the perturbation potential Eq. (36).

The configuration plots $|\psi_E(x,y)|^2$ (see Fig. 7) do not appear to contain this pendulum structure. This prompts us to examine the quantum counterpart of the classical Poincaré maps.

Appendix A gives the details of how we can construct quantum Poincaré plots using the well known Husimi distribution [28–30]. The quantum Poincaré plots associated with levels 1–4 (Fig. 8) and levels 19 and 20 (Fig.
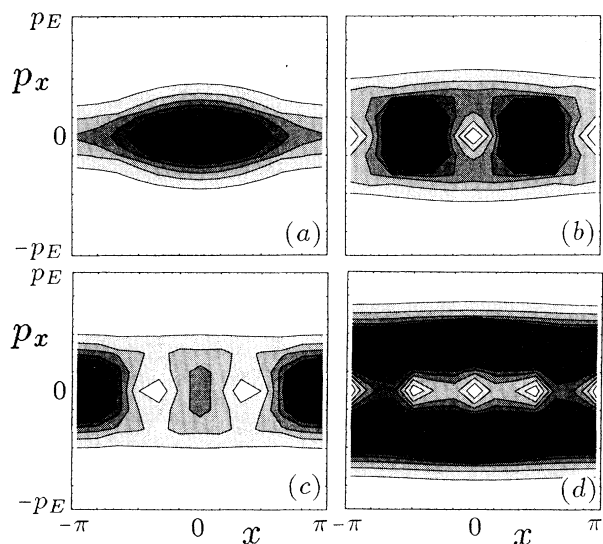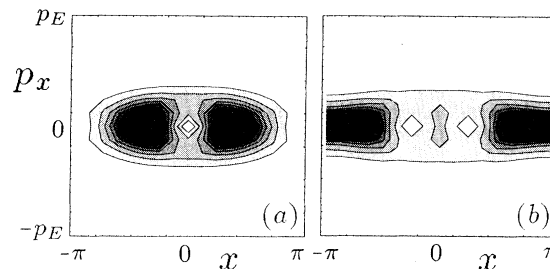
9) show that the quantum eigenstates for these levels are pendulumlike. For example, note the sequence 1–4 in Fig. 8. Levels 1 and 2 are libration states. Level 3 sits on the unstable periodic orbits and level 4 is a translation (rotation) state. We found that for the wide channel, agreement between QDTP and numerical experiments is good even when the classical phase space is mixed, such as in Fig. 3(b). We believe that for the wide channel, the resonance structure is too small to be resolved by the quantum system at low energy. It is important to note that the classical Poincaré maps are energy independent, whereas the quantum Poincaré maps each have different energy (for different eigenstates). In Appendix B, a simple semiclassical analysis is presented, which reveals that either by varying the physical size of the billiard for a fixed energy or by varying the energy for a given size of the billiard, we vary the degree to which the system exhibits classical or quantum behavior. In particular, as energy is increased (for fixed billiard size) the classical features are expected to manifest themselves more and more clearly. We shall show this in the following section.

V. LARGER RIPPLES AND HIGHER ENERGY

Let us consider first the band spectra of the narrow channel and ripple size $a = \frac{2\pi}{50}$ [Fig. 6(a)]. Notice the almost flat lower bands and the approximately equal spacing between them. The equidistance of spacing between levels reminds us of simple harmonic oscillator states. The classical Poincaré plot for these values is shown in Fig. 2(c). The classical phase space is that of a perturbed pendulum with a large resonance and a chaotic separatrix. Figure 10 shows the quantum Poincaré plots for the first eight levels, at $k = 0$. Here we see that only the first and second levels fall well within the classically regular region. The higher levels [see Figs. 10(c)–10(h)] lie predominantly on the largest librational orbits and on the chaotic separatrix [see Fig. 2(c)] of the large central resonance zone. We know that the level spacing between energy eigenstates in the region of libration for an integrable quantum pendulum *decreases* in the neighborhood of the separatrix. So how do we explain the rigid, almost constant spacing of energy levels? We believe we are see-

FIG. 8. Husimi plots for the narrow channel with $d = \frac{2\pi}{10}$, $a = \frac{2\pi}{1000}$, and $k = 0$. These correspond to energy levels (a) 1, (b) 2, (c) 3, and (d) 4 (in a.u.).

ing the effect of level repulsion (see, for example, Refs. [4, 18]) induced by the transition to chaos in the separatrix region. Notice that energy levels that are showing rigid structure have eigenstates that lie on or partly on the chaotic separatrix region.

Now let us consider the narrow channel with $a = \frac{2\pi}{25}$. The corresponding classical Poincaré plots and band structures are shown in Figs. 2(d) and 6(b), respectively. Here we wish to look at the higher energy states. The reason is that as the energy E increases, the coarse graining of the quantum Poincaré plots becomes finer and as argued in Appendix B, the quantum system should encounter more of the underlying classical structure. This is indeed the case, as a comparison between Figs. 2(d) and 11 shows. Note in Figs. 11(a) and 11(b) that energy levels 452 and 455 can resolve the period-8 resonance island chain surrounding the large resonance of Fig. 2(d). The energy level 452 has maximum probability precisely

on the stable (elliptic) fixed points in the chain. The energy level 455, on the contrary, has maximum probability on the unstable (hyperbolic) regions of the chain.

The states shown in Figs. 11(c)–11(f) are also at fairly high energy and lie in the chaotic sea of the classical Fig. 2(d). Figures 11(c) and 11(d) correspond to energy levels 403 and 418, respectively. They show strong evidence of "scarring." As Heller showed [5], it is not uncommon to find eigenstates with probability strongly peaked on the unstable periodic orbits in a chaotic sea. Although we have not searched for unstable periodic orbits in the chaotic sea of Fig. 2(d), we would not be surprised to find period-4 unstable periodic orbits at the locations of large probability in Fig. 11(d). Figures 11(e) and 11(f) correspond to levels 1001 and 1005, respectively. Note the finer detail that appears at these higher energy levels.

All of the Husimi plots shown so far have been for states with $k = 0$. These states all have definite parity, as can be seen from their symmetric distribution about $p_x = 0$. It is of interest also to look at states with $k \neq 0$. These states will not have definite parity and will have an unequal distribution of probability about $p_x = 0$. They can also be thought to represent states with a net momentum. Figures 12(a) and 12(b) show the fifth and sixth state at $k = \frac{1}{12} + 0.00005$ for the wide channel, with $a = \frac{2\pi}{300}$. At $k = \frac{1}{12}$ these levels avoid crossing. Note
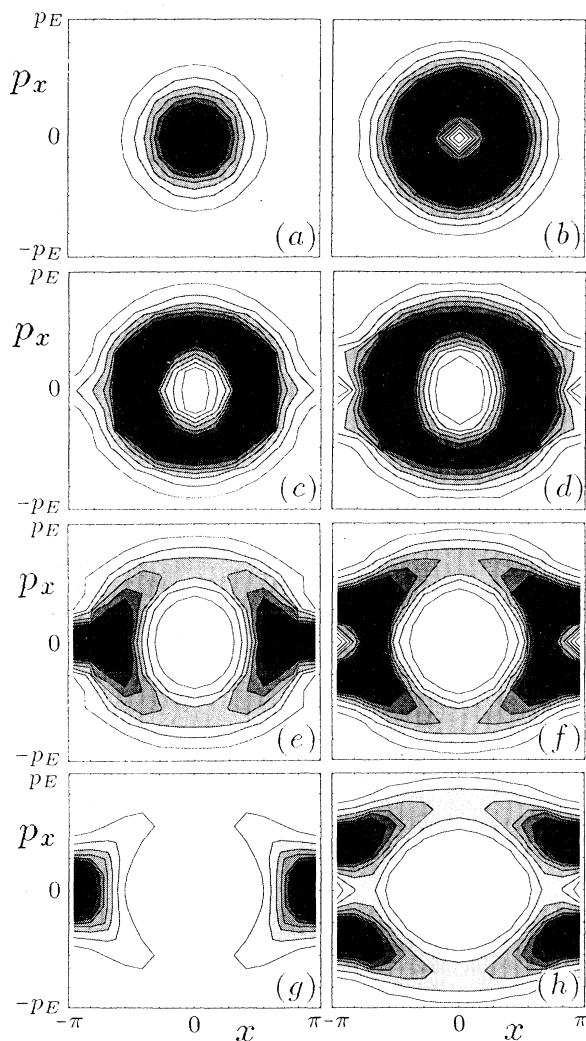

FIG. 10. Husimi plots for the narrow channel with $d = \frac{2\pi}{10}$, $a = \frac{2\pi}{50}$, and $k = 0$. (a)–(h) correspond to energy levels 1–8, respectively (in a.u.).
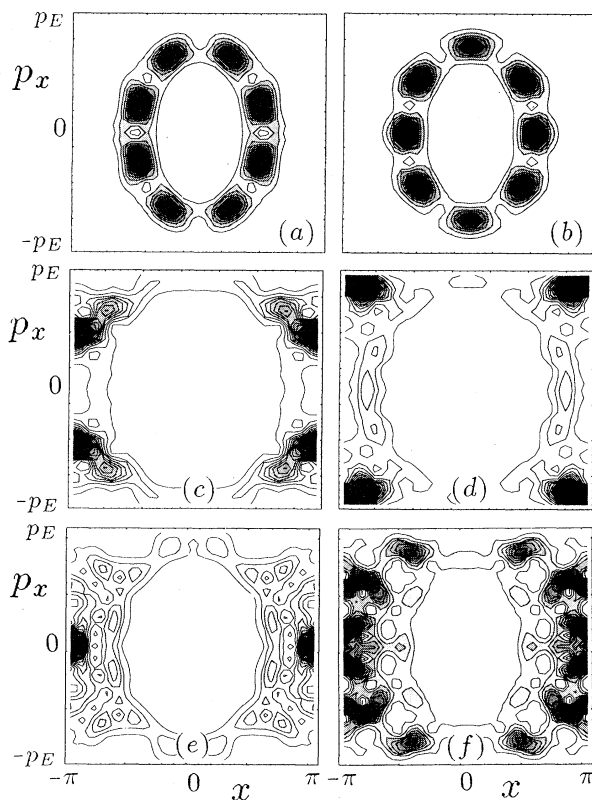

FIG. 11. Husimi plots for the narrow channel with $d = \frac{2\pi}{10}$, $a = \frac{2\pi}{25}$, and $k = 0$. These correspond to energy levels (a) 452, (b) 455, (c) 403, (d) 418, (e) 1001, and (f) 1005 (in a.u.).
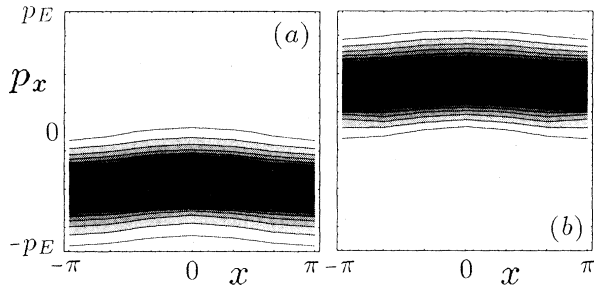
FIG. 12. Husimi plots for the wide channel with $d = 3\pi$, $a = \frac{2\pi}{300}$, and $k = \frac{1}{12} + 0.000\,05$. These correspond to energy levels (a) 5 and (b) 6. At $k = 1/12$, the fifth and sixth unperturbed states are degenerate; see Fig. 5(a) (in a.u.).

that the fifth state has negative net momentum and the sixth state has positive net momentum. This is consistent with the signs of the slopes at $k = \frac{1}{12} + 0.000\,05$, that is, negative for the fifth level and positive for the sixth level. The Husimi plots for the fifth and sixth states for k slightly less than $\frac{1}{12}$ are consequently reversed.

VI. CONCLUSION

We have reported here our studies of the classical and quantum versions of a particle confined in a rippled infinitely long two-dimensional channel. We analyze two representative geometries: a wide and a narrow channel. Their Poincaré surfaces of section for various ripple amplitudes revealed the rich classical dynamics of the system, with the typical mixed phase space of chaotic systems.

Quantum mechanically, it was found convenient to describe the motion in a curvilinear coordinate system, where the boundaries become flat but the Hamiltonian acquires coordinate and momentum dependent terms. This approach lends itself naturally to the numerical solution of the eigenvalue problem as well as to a perturbative treatment. For small ripples, quantum degenerate perturbation theory gives a picture of the particle moving inside a flat channel subject to a perturbation. The exact numerical values of the energy eigenvalues and the QDPT predictions were compared. For the wide channel, first-order QDPT gave correctly which crossings would remain degenerate and which ones repel as the perturbation was turned on. Moreover, first-order QDPT predicted correctly the amount of splitting of the avoided crossings. Such an agreement was found to be true (for the lower part of the energy spectrum) even for ripple sizes for which their corresponding classical Poincaré maps had a mixed phase space. In contrast, the avoided crossings and their magnitudes for the narrow channel disagreed strongly with QDPT to first order even for very small ripple sizes. The corresponding classical Poincaré map was found to be that of a minimally perturbed pendulum, the width of the chaotic separatrix practically zero, i.e., the map is quasiintegrable. Second-order QDPT showed that in order for the low-order predictions (weak binding approximation) to be valid not only must the ripple be

small but also the width of the channel must be large enough.

The disagreement with QDPT found for the narrow channel, where the corresponding classical map is quasi-integrable and the agreement for the wide channel for which the classical maps are chaotic, might be understood as follows. The lower part of the spectrum corresponds to the extreme quantum limit and as the energy is increased, the semiclassical limit is reached (see Appendix B). The classical features of the Poincaré map of the wide channel appear to be too small to be resolved by the quantum system at low energy. We believe this is why we find agreement between perturbation calculations and numerical results for the wide channel, apart from the fact that QDPT works for rather low levels only. On the other hand, the motion in the narrow channel is dominated by a large pendulumlike structure that can be resolved by the low-energy eigenstates. This was confirmed by the quantum Poincaré plots. Namely, the ground state at $k = 0$ lies inside the resonance island with maximum probability at the center, the second and third levels fall on the separatrix, the fourth falls barely outside the separatrix, and higher states correspond to translational modes. We have seen that *quantum perturbation theory, like classical perturbaton theory, must be used with caution.* One cannot disregard the underlying classical dynamics. Finally, the idea that higher energy states contain information about semiclassical behavior appears to be in agreement with the overall trend of our quantum Poincaré plots, which resolved more and more details and structures from the classical Poincaré plots as energy was increased.

APPENDIX A: HUSIMI PLOTS (28)–(30)

The Husimi distribution function [28] $H(x_0, p_{x0})$ can be viewed as a quantum mechanical phase space probability density for an arbitrary quantum state $|\Psi\rangle$. It is defined by

$$H(x_0, p_{x0}) = |\langle\Psi|x_0, p_{x0}\rangle|^2, \tag{A1}$$

where the state $|x_0, p_{x0}\rangle$ is a coherent state that can be represented in the position basis as

$$\langle x|x_0, p_{x0}\rangle = \left(\frac{\omega}{\pi\hbar}\right)^{1/4} \exp\left(-\frac{\omega}{2\hbar}(x - x_0)^2\right.$$
$$\left. +i\frac{p_{x0}}{\hbar}(x - x_0)\right). \tag{A2}$$

The coherent state has uncertainty $\sigma_x = \sqrt{\hbar/2\omega}$ in position and uncertainty $\sigma_p = \sqrt{\hbar\omega/2}$ in momentum and the wave packet is a minimum uncertainty wave packet $\sigma_x\sigma_p = \hbar/2$. The choice of the value of the coarse graining parameter ω is specified below.

Our system has two degrees of freedom and with energy conservation we have a three-dimensional phase space. We can obtain a quantum Poincaré surface of section (following the approach of Ref. [29]) if we use the fact that there is an approximate separation of variables near the boundary. Near $y = 0$, the wave function $\Psi(x, y)$ can be locally separated to first order,

$$\Psi(x, y)|_{y\approx0} = 0 + \frac{\partial}{\partial y}\Psi(x, y)|_{y=0} y + O(y)^2 + \cdots. \tag{A3}$$

We can define

$$S(x) \equiv \frac{\partial}{\partial y}\Psi_E(x, y)|_{y=0} = \sqrt{\pi}\sum_{m,n} B_{mn} m \frac{e^{i(n+k)x}}{(d + a\cos x)^{3/2}} \tag{A4}$$

(cf. Sec. III).

In the ripple channel, the coordinate x was chosen to have 2π periodicity. Therefore, we have used the periodic coherent state [30]

$$\langle x|x_0, p_{x0}\rangle = \left(\frac{\omega}{\pi\hbar}\right)^{1/4} \sum_{l=-\infty}^{\infty} \exp\left(-\frac{\omega}{2\hbar}(x + 2\pi l - x_0)^2\right.$$
$$\left. +i\frac{p_{x0}}{\hbar}(x + 2\pi l - x_0)\right). \tag{A5}$$

The Husimi distribution near the boundary $y \approx 0$ is given by

$$H(x_0, p_{x0})$$

$$= \left|\int dx\langle x_0, p_{x0}|x\rangle S(x)\right|^2$$

$$= \sqrt{\frac{\omega\pi}{\hbar}}\left|\int_0^{2\pi} dx' \sum_{l=-\infty}^{\infty} \frac{\exp\left[i\frac{p_{x0}}{\hbar}(x + 2\pi l - x_0)\right]}{\exp\left[\frac{\omega}{2\hbar}(x + 2\pi l - x_0)^2\right]}\right.$$

$$\left. \times \sum_{m,n} B_{mn} m \frac{e^{i(n+k)x}}{(d + a\cos x)^{3/2}}\right|^2. \tag{A6}$$

In each Husimi plot, the x axis has the range $-\pi \leq x \leq \pi$ (one period of the ripple). For each energy eigenstate, we chose the momentum cutoff to be $p_E = \sqrt{2E}$ (unless stated otherwise), where E is the energy of the eigen-

state. In all Husimi plots presented here, ω is chosen so that the coarse graining is symmetrical in phase space, as in Ref. [29]. That is, it is obtained by requiring that $2p_E/\sigma_p = 2\pi/\sigma_x$. This gives $\omega = p_E/\pi$. In our system, quantum mechanically we cannot define sharp values for the momentum and energies simultaneously. In cases where the probability extended beyond $p_E = \sqrt{2E}$ in momentum space, the plots were extended to larger values of p_x.

APPENDIX B: SEMICLASSICAL FLAT-CHANNEL BILLIARD

It is of interest to look at the billiard from the viewpoint of semiclassical quantization. Let us consider a rectangular billiard with length L in the x direction and length d in the y direction. Let us assume periodic boundary conditions in the x direction. This makes it a flat channel. Assume that a trajectory has momentum components $p_x = p\sin(\alpha)$ and $p_y = p\cos(\alpha)$ and kinetic energy $E = p^2/2m$, where m is the mass of the particle, p is the magnitude of the momentum, and α is the angle the orbit makes with the y axis. The actions associated with the motions in the x and y directions are

$$J_x = \frac{1}{2\pi}\oint p_x dx = \frac{p_x L}{2\pi} = \frac{pL}{2\pi}\sin(\alpha),$$

$$J_y = \frac{1}{2\pi}\oint p_y dy = \frac{p_y d}{\pi} = \frac{pd}{\pi}\cos(\alpha). \tag{B1}$$

It is important to note that the classical billiard is allowed to have any energy and for each energy there is a continuous range of possible motions for as small a spatial scale as desired. In the surfaces of section in Figs. 2 and 3, all the trajectories, regular and chaotic, in a given plot have the same total kinetic energy.

The quantum system is quite different and we can see this if we quantize the action. That is, we let $J_x = n_x\hbar$ and $J_y = n_y\hbar$, where n_x and n_y are integers (but not both zero) and $\hbar$ is Planck's constant. It is also useful to rewrite all quantities in terms of atomic units. We let $p = p_0\frac{\hbar}{a_B}$ and $m = m_0 m_e$, where a_B is the Bohr radius and m_e is the mass of the electron. Then the kinetic energy $E = E_0 E_B = \frac{p_0^2}{2m_0}E_B$, where $E_B = \frac{\hbar^2}{m_e a_B^2}$ is twice the ionization energy of the hydrogen atom. Also, the size of the system can be expressed in multiples of the Bohr radius $L = L_0 a_B$ and $d = d_0 a_B$. From the quantization condition on the action it is easy to show that

$$p_0 = \sqrt{\frac{4\pi^2 n_x^2}{L_0^2} + \frac{\pi^2 n_y^2}{d_0^2}}. \tag{B2}$$

Therefore,

$$\sin(\alpha) = \left(\frac{2\pi n_x}{L_0}\right)\bigg/\sqrt{\frac{4\pi^2 n_x^2}{L_0^2} + \frac{\pi^2 n_y^2}{d_0^2}}. \tag{B3}$$

From these equations, we see that the classical or quan-

tum nature of the system depends drastically on the physical size of the system for a given energy. Let us consider a small billiard such that $L_0 = 2\pi$ and $d_0 = \pi$. Then

$$\sin(\alpha) = \frac{n_x}{\sqrt{n_x^2 + n_y^2}}. \qquad \text{(B4)}$$

For low energies, the angles of the allowed orbits are quantized. Therefore, the low energy states in a channel of small physical size (of order of the hydrogen atom)

cannot distinguish the underlying complicated motions of the classical system.

From this analysis we see that by varying the physical size of the billiard for a given energy or by varying the energy for a given size of the billiard, we vary the degree to which the system exhibits a classical or quantum type of behavior. For a billiard of a fixed size, the higher the energy, the closer the quantum system will come to semiclassical behavior.

[1] Ya. G. Sinai, Usp. Math. Nauk **25**, 137 (1970) [Russ. Math Surv. **25**, 137 (1970)].

[2] L.A. Bunimovich, Funct. Anal. Appl. **8**, 254 (1974); Chaos **1**, 187 (1992).

[3] See A.M. Ozorio de Almeida, *Hamiltonian Systems: Chaos and Quantization* (Cambridge University Press, New York, 1988); P.J. Richens and M.V. Berry, Physica D **2**, 495 (1981).

[4] M. V. Berry, Ann. Phys. (N.Y.) **131**, 163 (1981); O. Bohigas, M.J. Giannoni, and C. Schmidt, Phys. Rev. Lett. **52**, 1 (1984).

[5] S. W. McDonald and S.N. Kauffman, Phys. Rev. A **37**, 3067 (1988); M.V. Berry, Proc. R. Soc. London Ser. A **400**, 229 (1988); E.J. Heller, Phys. Rev. Lett. **53**, 1515 (1984); S. Tomsovic and E.J. Heller, *ibid.* **70**, 1405 (1993); M.V. Berry in *Chaotic Behavior of Deterministic Systems*, 1993 Les Houches Lectures Session XXXVI, edited by G. Iooss, R.H.G. Helleman, and R. Stora (North-Holland, Amsterdam, 1983), p. 172.

[6] R.A. Jalabert, H.U. Baranger, and A.D. Stone, Phys. Rev. Lett. **65**, 2442 (1990); H.U. Baranger, D.P. Vincenzo, R.A. Jalabert, and A.D. Stone, Phys. Rev. B **44**, 10 637 (1991).

[7] K.L. Shepard, M.L. Roukes, and B.P. Van der Gaag, Phys. Lett. **68**, 2660 (1992); M.L. Roukes and O.L. Alerhand, *ibid.* **65**, 1651 (1990).

[8] D. Mailly, C. Chapelier, and A. Benoit, Phys. Rev. Lett. **70**, 2020 (1993).

[9] C. M. Marcus, A.J. Rimberg, R.M. Westervelt, P.F. Hopkins, and A.C. Gossard, Phys. Rev. Lett. **69**, 506 (1992).

[10] M. Robnik and M.V. Berry, J. Phys. A **18**, 1361 (1985); K. Nakamura and H. Thomas, Phys. Rev. Lett. **61**, 247 (1988).

[11] V. Stoffregen, J. Stein, H.-J. Stockmann, M. Kus, and F. Haake, Phys. Rev. Lett. **74**, 2666 (1995); (wave chaos experiment) P. So, S.U. Anlage, E. Ott, and R.N. Oerter, *ibid.* **74**, 2662 (1995).

[12] L.P. Kouwenhoven *et al.*, Phys. Rev. Lett. **65**, 361 (1990).

[13] C.S. Lent and M. Leng, J. Appl. Phys. **70**, 3157 (1991).

[14] G. Timp, R. Behringer, S. Sampere, J.E. Cunningham, and R.E. Howard, in *Nanostructure Physics and Fabrication*, edited by M.A. Reed and W.P. Kirk (Academic, New York, 1989), p. 331.

[15] S. Yu. Potapenko and A.M. Satanin, Phys. Status Solidi B **123**, 191 (1984).

[16] G.A. Luna-Acosta, A. Krokhin, M.A. Rodriguez-Meza, and P.H. Hernandez-Tejeda, in *Chaos in Mesoscopic Systems*, edited by H. Cerdeira and G. Casati (World Scientific, Singapore, in press).

[17] V. Ya. Demikhovskii, S. Yu. Potapenko, and A.M. Satanin, Fiz. Tekh. Poluprovodn. **17**, 213 (1983) [Sov. Phys. Semicond. **17**, 137 (1983)].

[18] L.E. Reichl, *The Transition to Chaos in Conservative Classical Systems: Quantum Manifestations* (Springer-Verlag, New York, 1992); F. Haake, *Quantum Signatures of Chaos* (Springer-Verlag, Berlin, 1991).

[19] M.C. Gutzwiller, *Chaos in Classical and Quantum Mechanics* (Springer-Verlag, New York, 1990); K. Nakamura, *Quantum Chaos: a New Paradigm on Nonlinear Dynamics* (Cambridge University Press, New York, 1993).

[20] E.R. Mucciolo, R.B. Capaz, B.L. Altshuler, and J.D. Joannopoulos, Phys. Rev. B **50**, 8245 (1994).

[21] A.J. Lichtenberg and M.A. Lieberman, *Regular and Stochastic Motion* (Springer-Verlag, New York, 1982), Sec. (6.1b); J.L. Tennyson in *Nonlinear Dynamics and the Beam-Beam Interaction*, edited by M. Month and J.C. Herrera, AIP Conf. Proc. No. 57 (AIP, New York, 1979), p. 272.

[22] B.S. DeWitt, Rev. Mod. Phys. **29**, 377 (1957).

[23] R. Adler, M. Bazin, and M. Schiffer, *Introduction to General Relativity* (McGraw-Hill, New York, 1975).

[24] A.E. Meyerovich and S. Stepaniants, Phys. Rev. Lett. **73**, 316 (1994).

[25] See, e.g., R.L. Ingraham, *A Survey of Nonlinear Dynamics "Chaos Theory,"* (World Scientific, Singapore, 1992), Sec. (7.4).

[26] L.D. Landau and E.M. Lifshitz, *Quantum Mechanics. Non-Relativistic Theory* (Pergamon, New York, 1977), Sec. 39.

[27] P.M. Morse and H. Feshback, *Methods of Theoretical Physics* (McGraw-Hill, New York, 1953), Table 9.1, p. 1010.

[28] K. Husimi, Proc. Phys. Math. Soc. (Jpn.) **22**, 246 (1940).

[29] B. Crespi, G. Perez, and S.-J. Chang, Phys. Rev. E **47**, 986 (1993).

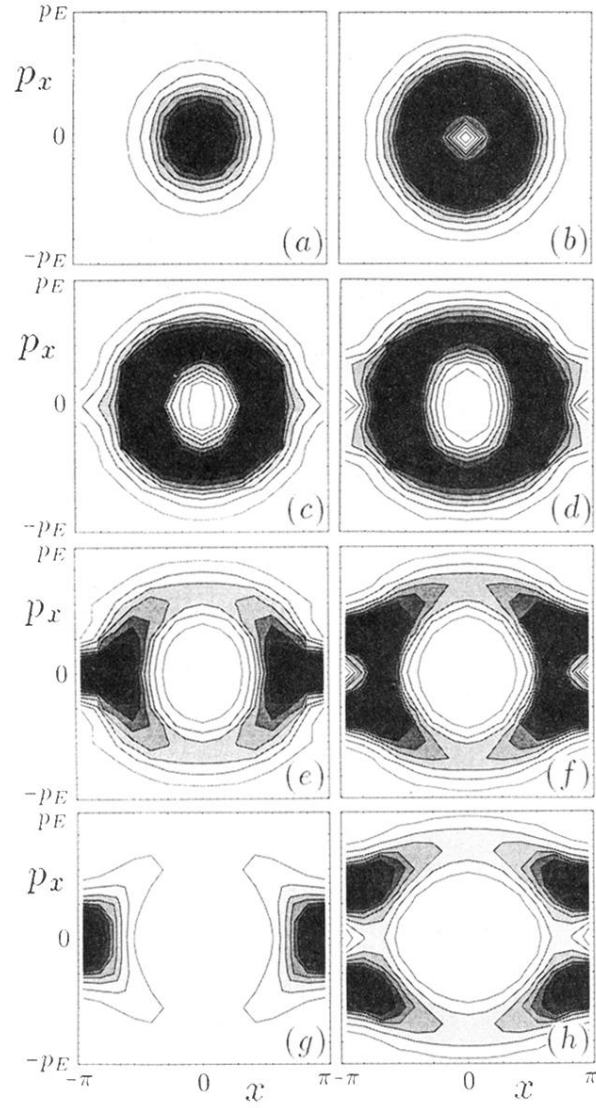[30] S.-J. Chang and K.-J. Shi, Phys. Rev. A **34**, 7 (1986).

FIG. 10. Husimi plots for the narrow channel with $d = \frac{2\pi}{10}$, $a = \frac{2\pi}{50}$, and $k = 0$. (a)–(h) correspond to energy levels 1–8, respectively (in a.u.).
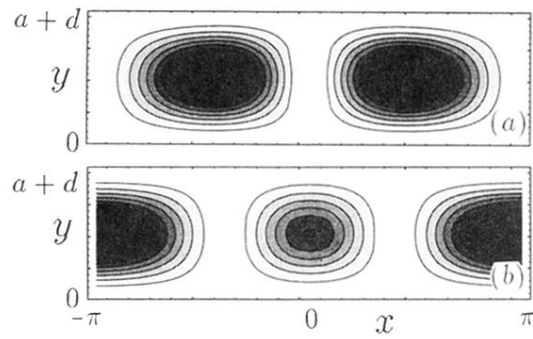
FIG. 7. Energy eigenstates in the x-y plane for the narrow channel with $d = \frac{2\pi}{10}$, $a = \frac{2\pi}{1000}$, $\epsilon = 0.01$, and $k = 0$. These correspond to energy levels (a) 2 and (b) 3 (in a.u.).
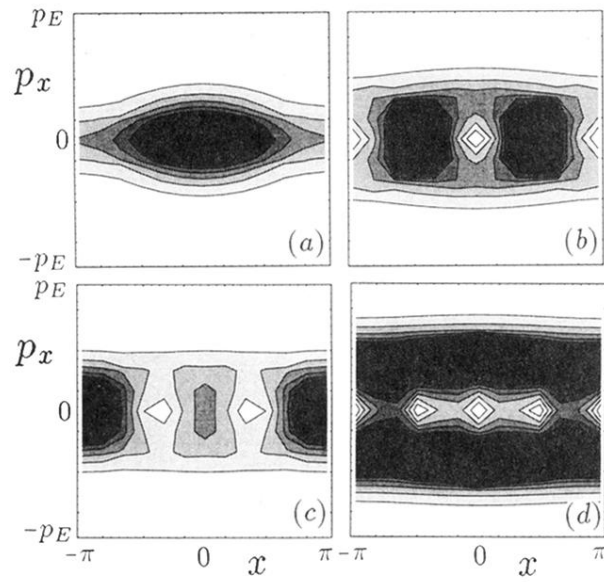
FIG. 8. Husimi plots for the narrow channel with $d = \frac{2\pi}{10}$, $a = \frac{2\pi}{1000}$, and $k = 0$. These correspond to energy levels (a) 1, (b) 2, (c) 3, and (d) 4 (in a.u.).
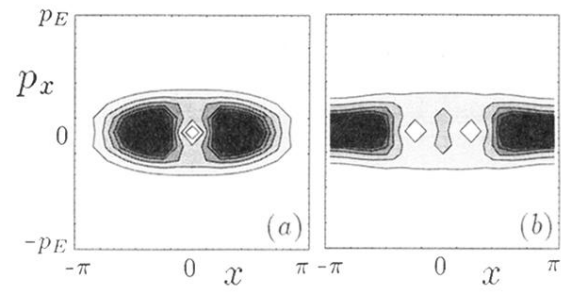
FIG. 9. Husimi plots for the narrow channel with $d = \frac{2\pi}{10}$, $a = \frac{2\pi}{1000}$, and $k = 0$. These correspond to energy levels (a) 19 and (b) 20 (in a.u.).